# Gadolinium-loaded Plastic Scintillators for Thermal Neutron Detection using Compensation

Jonathan Nicolas Dumazert, Romain Coulon, Matthieu Hamel, Frédérick Carrel, Fabien Sguerra, Stéphane Normand, Laurence Méchin, Guillaume H. V. Bertrand

# Gadolinium-loaded plastic scintillators for thermal neutron detection using compensation

Jonathan Dumazert*, Romain Coulon, Matthieu Hamel, Frédérick Carrel, Fabien Sguerra, Stéphane Normand, Laurence Méchin and Guillaume H. V. Bertrand.

***Abstract* – Plastic scintillator loading with gadolinium-rich organometallic complexes shows a high potential for the deployment of efficient and cost-effective neutron detectors. Due to the low-energy photon and electron signature of thermal neutron capture by Gd-155 and Gd-157, alternative treatment to pulse-shape discrimination has to be proposed in order to display a count rate. This paper discloses the principle of a compensation method applied to a two-scintillator system: a detection scintillator interacts with photon and fast neutron radiation and is loaded with gadolinium organometallic compound to become a thermal neutron absorber, while a not-gadolinium loaded compensation scintillator solely interacts with the fast neutron and photon part of incident radiation. After the nonlinear smoothing of the counting signals, a hypothesis test determines whether the resulting count rate post-background response compensation falls into statistical fluctuations or provides a robust indication of neutron activity. Laboratory samples are tested under both photon and neutron irradiations, allowing the authors to investigate the performance of the overall detection system in terms of sensitivity and detection limits, especially with regards to a similar-active volume He-3 based commercial counter. The study reveals satisfactory figures of merit in terms of sensitivity and directs future investigation toward promising paths.**

## I. Introduction

NEUTRON counting forms a critical branch of nuclear-related issues, whether flow monitoring on industrial infrastructures, dose rate monitoring for radioprotection or radiological material detection addressing CBRN threats [1] are concerned. More specifically, the last decade has been driven by the quest for competitive alternative technologies to neutron counters based on the He-3 isotope, whose announced worldwide shortage has generated massive market value fluctuations [2]. In the meantime, the loading of plastic scintillators with gadolinium-rich organometallic complexes shows a high potential for the deployment of efficient and cost-effective detectors [3]. Natural gadolinium, through its 155 and (especially) 157 isotopes, exhibits the largest cross section (48890 barns [4]) available among stable elements for the absorption of incident neutrons within the thermal energy range. A technical conundrum lies within the separation of the scintillation signal from prompt gamma rays emitted after the (n,γ) neutron radiative capture from the scintillation signal attributable to ambient gamma-rays and falling into the same energy range. In default of any available pulse-shape discrimination (PSD), the authors propose a neutron counting method on the basis of a robust compensation technique.

Manuscript received February 23rd 2016.

Jonathan Dumazert, Romain Coulon, Matthieu Hamel, Frédérick Carrel, Stéphane Normand and Guillaume H. V. Bertrand are with CEA, LIST, Laboratoire Capteurs et Architectures Electroniques, 91191 Gif-sur-Yvette, France (telephone: +33(0)169085324, e-mail: jonathan.dumazert@cea.fr).

Laurence Méchin is with CNRS (UMR6072), UCBN, ENSICAEN, Groupe de Recherche en Informatique, Image, Automatique et Instrumentation de Caen, 14050 Caen, France.

## II. Related Work

Neutron detection represents a long-term technological challenge due to the indirectly ionizing nature of the radiation: the secondary particles generated after an interaction between a neutron and an atom of the sensor, which carry a charge, actually form the signature of the neutron presence. It is additionally imperative, when monitoring neutron activity, to discriminate this signature against the signal generated by secondary particles generated through the interaction between background photon radiation and the electrons of the sensor atoms.

Among the detectors specifically dedicated to thermal neutrons, He-3 counters, which exploit a (n,p) type reaction with a thermal cross section equal to 5327 barns, are the most widespread [5]. Given the announced global shortage and strategic issues regarding tritium, alternative technologies to He-3 are actively investigated, notably among plastic scintillators [6], which are low-cost (contrary to inorganic scintillators), easily scalable and shape-flexible, safer than their liquid counterparts due to their higher flash point. A straightforward exploitation of plastics quantifies the energy laid down by recoil protons [7] along the diffusion of incident fast neutrons. In order to increase the sensitivity to thermal neutron radiation, these plastics have to be loaded with neutron adsorbing dopants, mainly B-10 or Li-6 [8-9]. While these isotopes, as alpha particle emitters following neutron capture, allow a PSD between neutron and photon-generated pulses (the background photon signature being essentially formed of low-energy electrons and photons), their absorption thermal cross section, respectively equal to 3840 and 950 barns, is significantly lower than the one of their He-3 competitor.

As already mentioned, natural gadolinium presents a 48890 barns cross section for the radiative (n,γ) capture of neutrons at 25 meV (ambient temperature). Plastic scintillator loading with pure gadolinium or gadolinium-rich organometallic compounds aims at exploiting this exceptionally high cross section [10-11]. A major technical difficulty lies within the separation of the scintillation signal attributable to recoil electrons in the plastic matrix, generated after an interaction with electrons or photons present in the (n,γ) cascade, from recoil electrons due to an interaction with background photons of comparable energy. Such drawback has motivated the authors of a reference patent application [12] to limit the scope

of their invention, including gadolinium-loading, to configurations in which PSD remains possible. As an alternative to this approach, we hereby propose the transposition to gadolinium-based detection of a well-known measurement method in plastic scintillation [13-14], in which one makes use of two separate plastic scintillators with one them being, for instance, loaded with B-10 or Li-6 to be turned into a thermal neutron-sensitive detector, while the unloaded second one remains solely sensitive to other types of radiations.

## III. Principle of a Detection Method Using Photon Response Compensation

The principle of the neutron activity monitoring system disclosed is currently under patent deposition [15]. It is based on a two-scintillator compensation system:

- the first scintillator, named *detection scintillator*, interacts with fast neutrons and photon radiations, and is loaded with gadolinium to become a thermal neutron absorber as well ;
- the second scintillator, named *compensation scintillator*, is not-gadolinium loaded and therefore thermal neutron-insensitive.

The signature of the interaction between thermal neutrons and gadolinium may then be isolated by subtracting the compensation scintillator response to the total detection scintillator response, weighted by a coefficient representing their relative responses to fast neutrons and photon radiations.

### *A. Photon and electron signature of thermal neutron radiative capture by Gd-157 and Gd-155*

Natural gadolinium (Gd) exists in the form of a combination of isotopes among which Gd-155 (14.8 % proportion, 60900 barns cross section) and mostly Gd-157 (15.65 %, 254000 barns) present an exceptionally high interaction probability with thermal neutrons [4].

The prompt source term associated with the de-excitation of a gadolinium following the absorption of a thermal neutron is subdivided into a prompt photon source term and a prompt electron source term. The complete equations of the nuclear reactions are presented in Eq. (1) and (2), where the sum of the gamma-rays labeled $\gamma$ and the X-rays noted $RX$ forms the photon source term, and the sum of internal conversion electrons noted $CIe^-$ and the labeled Auger electrons $Ae^-$ forms the electron source term.

$$^{155}_{64}\mathrm{Gd} + {}^{1}_{0}n \rightarrow {}^{156}_{64}\mathrm{Gd}^{*} \rightarrow {}^{156}_{64}\mathrm{Gd} + \gamma + RX + CIe^- + Ae^- \quad (1)$$

$$^{157}_{64}\mathrm{Gd} + {}^{1}_{0}n \rightarrow {}^{158}_{64}\mathrm{Gd}^{*} \rightarrow {}^{158}_{64}\mathrm{Gd} + \gamma + RX + CIe^- + Ae^- \quad (2)$$

As we primarily aim at the deployment of small and medium-volume scintillators (e.g. 1 to 10 cm height and diameter), the exploitable signature is limited to the most significant electron terms and few hundred keV photon terms, which will significantly interact inside the sensors and thus induce a measurable scintillation signal. For the $^{157}_{64}\mathrm{Gd}(n,\gamma)$ radiative capture, the significant $\gamma$ are emitted at 79.51 keV (0.773 per neutron capture abbreviated nc) and 181.93 keV (1.39 / nc) [16], together with the significant $CIe^-$ associated with the ray at 29.27 keV (0.348 / nc) [17] and accompanying X-rays [16] between 5 and 50 keV. For the $^{155}_{64}\mathrm{Gd}(n,\gamma)$ radiative capture, the significant $\gamma$ are emitted at 88.967 keV (0.266 / nc) and 199.21 keV (0.389 / nc) [16], together with the significant $CIe^-$ associated with the ray at 38.73 keV (0.107 / nc) [17] and accompanying X-rays [16] between 5 and 50 keV.

A characteristic spectral distribution of the statistical signature of a thermal neutron flux into a 2 wt% gadolinium-loaded plastic scintillator is simulated using the probabilistic MCNPX2.7 Monte Carlo code for particle transport [18]. The program simulates a complete history of every generated corpuscle, for source terms as well as for diffusion products, until its energy falls below a 1 keV threshold.

The modeled natural plastic scintillator has the simplified form of a 1.2 g.cm$^{-3}$ density 83.3 wt% carbon, 7.6 wt% hydrogen, 6.9 wt% oxygen, 0.2 wt% nitrogen and 2 wt% gadolinium $h = 8$ mm height and $d = 17.5$ mm diameter perfect cylinder using the MCNPX2.7 benz.01t material card to account for the styrene structure of the matrix. These parameters represent the scintillator used in Section VI for experimental investigation.

For Gd-155 and 157 isotopes respectively, photon and electron source terms following a homogenous spatial distribution are generated inside the scintillator using the IAEA database for the totality of the prompt gamma-rays and the BRICC database for the main internal conversion electrons with associated X-rays and Auger electrons. Eventually, using the deposition pulse height tally 8 of the MCNPX2.7 code, the spectrum of photon and electron actual energy deposition inside the gadolinium-loaded plastic scintillator is derived. These rates are respectively labeled $\tau_{D,157}$ and $\tau_{D,155}$ for the de-excitation source terms associated with Gd-157 and 155, and expressed in deposition rate per source term (d.t$^{-1}$). The overall $\tau$ typical spectrum for the signature deposition for the detection reads

$$\tau = \frac{\alpha.\tau_{D,157} + \beta.\tau_{D,155}}{\alpha + \beta} \quad (3)$$

with the $\alpha$ and $\beta$ weighting coefficients being computed as the products of isotopic importance and cross section. The spectral distribution from the simulated radiative capture inside the modeled gadolinium-loaded scintillator, which is displayed in Fig. 1, confirms that the energy deposition from the de-excitation signature predominantly lies under 200 keV, with peaks corresponding to the couple of gamma-rays, internal conversion electrons and X-rays discussed above.

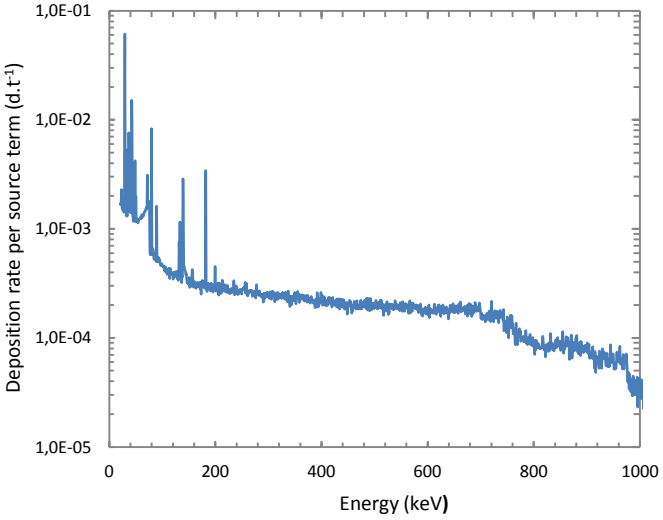


Fig. 1. Spectral distribution of radiative capture photon and electron signature in gadolinium-loaded plastic scintillator.

Given the typical energy resolutions expected for the real plastic scintillator samples [19], typically of the order of 10 keV, we shall group these signatures into two energy windows $F_1 = [0; 100\ \text{keV}]$ and $F_2 = [100\ \text{keV}; 200\ \text{keV}]$ over which selective countings should thus allow thermal neutron detection.

### B. *Detail of the system*

The detection and compensation part of the device is represented by two equal-volume plastic scintillators, which may be concentric (for instance, two cylinders or spheres with the same symmetry axis) or not-concentric and with the same geometry. In that last case, which is investigated in the present paper, both scintillators may be set side by side as depicted in Fig. 2 or head to tail. The detection scintillator (1) is loaded with gadolinium, under organometallic compound form, while the compensation scintillator (2) is not-gadolinium loaded.

Both scintillators are covered with diffusers (3) such as white paint or Teflon so that as many scintillation photons as possible are collected. Both channels are isolated by a suitably dimensioned attenuator (typically lead) thickness (4), inserted in between them so that X- and gamma-rays generated inside (1) and forming the exploited signature of a neutron capture induce as few false counts in (2) as possible. Both scintillators may optionally be isolated from photon background radiation by a lead or steel shield (5), in order to maximize the signal-to-noise ratio, completed by a moderating material for incident neutrons such as a thickness of polyethylene. The conversions of the scintillation photons from (1) and (2) are respectively performed at the entrances of the photomultiplier tubes (6) and (7). The acquisition and treatment of the photoelectronic signals from (6) and (7) are achieved by dedicated electronics (8) connected to a software and interface (9).

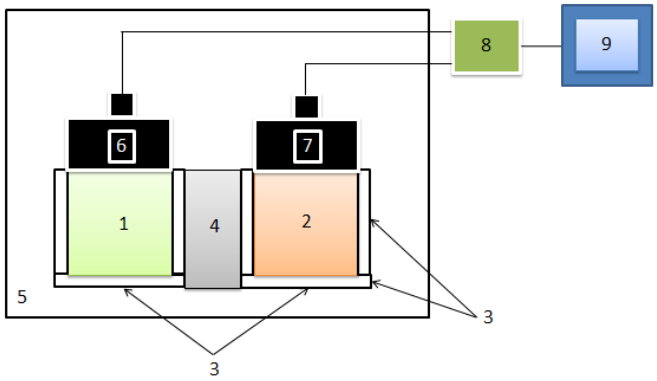


Legend:
1: Detection gadolinium-loaded plastic scintillator
2: Compensation plastic scintillator
3: White paint reflector
4: Lead insulator
5: Shield / moderator
6: Photomultiplier tube
7: Photomultiplier tube
8: Electronic chain
9: Software

Fig. 2. Principle sketch of the detection system.

The treatment of scintillation pulses includes amplitude triggering, bin-to-bin subtraction of the energy spectra acquired on the detection channel (channel 1) and the compensation channel (channel 2), integration of the spectral difference over energy windows of interest in order to isolate the signature of thermal neutron capture in the detection scintillator. The construction and parameterization of the hypothesis test for neutron detection is thoroughly described in Section V.

## IV. Estimation of the Photon Response Compensation Coefficient for Small-Volume Same-Geometry Gadolinium and Bismuth Loaded Plastic Scintillators

To investigate the concept of the neutron detection method exposed in section III, the neutron and photon radiation responses of small-volume same-geometry gadolinium-doped and not-gadolinium doped scintillating samples are assessed in terms of neutron counting over the full spectra and energy ranges $F_1 = [0; 100\ \text{keV}]$ and $F_2 = [100\ \text{keV}; 200\ \text{keV}]$.

### A. *Scintillating samples and acquisition setup*

The gadolinium-loaded plastic scintillators are prepared as described by Bertrand et al. [20] and comprise:

- a reticulated polystyrene matrix;
- a reticulating agent;
- 2,5-diphenyloxazole (PPO) as a primary fluorophore;
- 1,4-Bis((2-methylstyryl)benzene) (Bis-MSB) as a secondary fluorophore;
- gadolinium tris-tetramethylheptanedionate ($Gd(TMHD)_3$) as a gadolinium-rich organometallic compound.

The not-gadolinium loaded plastic scintillators for compensation may be prepared following the same recipe without the incorporation of $Gd(TMHD)_3$. However, the difference between the density and effective atomic number of

gadolinium-loaded and not-gadolinium loaded samples is responsible for a dramatic dependence of the $Q$ ratio of the counts registered in both scintillators with photon radiation energy for low energy radiation, mainly due to photoelectric effects [21], this dependence then disappearing for higher energy incident radiation. For the compensation to be easily implementable in photon backgrounds of versatile energy distribution, the coefficient $Q$ should be as little dependent on the incident photon energy as possible over the widest energy range. MCNPX2.7 simulations have shown that, for equal-volume scintillators, a significant decrease, reaching one order of magnitude, of the ratio between the maximum and the convergence value of $Q$ may be achieved by introducing moderate bismuth loading of the not-gadolinium loaded scintillator devoted to photon response compensation. This reduction is explained by the elevation of the effective atomic number of the resulting sample. The bismuth-loaded plastic scintillators are prepared with the same components as their gadolinium-loaded counterparts, except for the organometallic compound which is replaced by triphenyl bismuth ($BiPh_3$).

As far as the quantitative compositions of the not-loaded, gadolinium-loaded and bismuth-loaded scintillator are concerned, the authors use the notations A, B and C and the compositions described in Table I.

TABLE I. COMPOSITION OF PLASTIC SCINTILLATORS A, B AND C

| PS | $m_{monomers}$ (mg) | $m_{PPO}$ (mg) | $m_{Bis\text{-}MSB}$ (mg) | $m_{dopant}$ (mg) | wt% (metal) |
|---|---|---|---|---|---|
| A | 2910 | 90 | 0.9 | 0 | 0 |
| B | 2625 | 85 | 0.9 | 290 ($Gd(TMHD)_3$) | 2 (Gd) |
| C | 2240 | 690 | 0.9 | 70 ($BiPh_3$) | 0.8 (Bi) |

The scintillating samples are then cut into a cylindrical shape and polished so that they meet the desired dimensions, i.e. 17.5 mm diameter and 8 mm height. Their lateral surface is ultimately covered with diffusing white paint to limit the escape of scintillation photons.

Pulse height spectra are acquired using a Hamamatsu™ H1949-51 photomultiplier powered by an Ortec™ 556 High Voltage supply. Output signals are recorded unfiltered with a custom made acquisition setup developed in the laboratory. The photomultiplier is isolated from ambient light and static noise sources inside an opaque Faraday cage.

### *B. Nonlinear energy calibration of the scintillators*

In order to implement the photon response compensation of countings selectively registered over the energy windows $F_1 = [0; 100\ \text{keV}]$ and $F_2 = [100\ \text{keV}; 200\ \text{ke}V]$, it is necessary, for each of the prepared samples A, B and C, to establish a correspondence between every channel in which counts are displayed and an energy value. As preliminary observations, notably reported by Bertrand et al., have shown that the calibration coefficient associating one energy value to one channel number, is not constant over $F_1$ and $F_2$ (a typical phenomenon at low energy, as for instance described by Williamson et al. [22]), but varies instead with the incident photon energy, we performed a nonlinear calibration of the three scintillators by making use of several gamma radiation sources available in the laboratory, positioned at a distance $d = 10$ cm of the scintillator surface along the symmetry axis of the scintillator:

- an Am-241 source, whose activity as registered by the scintillator is dominated by a single $E_{\gamma,^{241}\text{Am}} = 59\ \text{keV}$ ray whose photoelectric peak is directly observed at $E_{PP,^{241}\text{Am}} = 59\ \text{keV}$ ;
- a Co-57 source, whose activity as registered by the scintillator is dominated by a single $E_{\gamma,^{57}\text{Co}} = 122\ \text{keV}$ ray whose photoelectric peak is directly observed at $E_{PP,^{57}\text{Co}} = 122\ \text{keV}$ ;
- a Cs-137 source, whose activity as registered by the scintillator is dominated by a single $E_{\gamma,^{137}\text{Cs}} = 662\ \text{keV}$ ray whose Compton edge is observed at $E_{CE,^{137}\text{Cs}} = 478\ \text{keV}$ ;
- a Na-22 source, whose activity as registered by the scintillator is dominated by a couple $E_{\gamma_1,^{22}\text{Na}} = 511\ \text{keV}$ and $E_{\gamma_2,^{22}\text{Na}} = 1275\ \text{keV}$ of rays, whose Compton edges are respectively observed at $E_{CE_1,^{22}\text{Na}} = 341\ \text{keV}$ and $E_{CE_2,^{22}\text{Na}} = 1057\ \text{keV}$.

Due to the small volume of the scintillators (about 2 $cm^3$) and the moderate mass load of heavy elements, respectively 2 wt% gadolinium for B and 0.8 wt% bismuth for C, it was impossible to observe the photoelectric peaks associated with the rays of Cs-137 and Na-22, hence the use of the respective Compton edges of these rays for calibration.

The experimental points are joined by line segments and the channel numbers respectively associated to both boundaries 100 keV and 200 keV are reported over one of these segments with uncertainties derived from the uncertainties attached to the closest experimental values. The three calibration curves are superimposed on Fig. 3 with a semi-logarithmic scale.

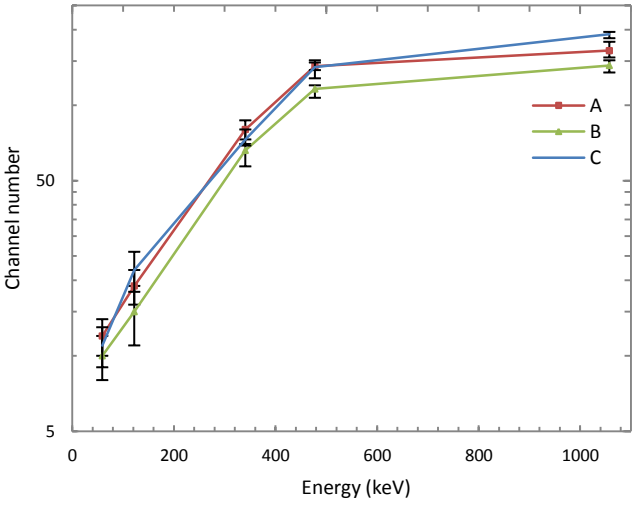


Fig. 3. Energy calibration curves of scintillators A, B and C.

*C. Comparison between simulated and experimental photon radiation compensation coefficients*

Let $N_A, N_B$ and $N_C$ be respectively the counts registered with scintillators A, B and C separately in the presence of a given photon radiation source, the simulation study presented in Section V showing that there is no expected significant bias in estimating the compensation coefficients for a photon background with the scintillators tested separately or side-by-side with a suitably dimensioned insulator in-between. These countings may be performed over the full energy spectra, i.e. all recording channels, or selectively over energy windows $F_1 = [0; 100\ \text{keV}]$ and $F_2 = [100\ \text{keV}; 200\ \text{keV}]$.

We introduce the notations $Q_{B/A} = \frac{N_B}{N_A}$ and $Q_{B/C} = \frac{N_B}{N_C}$. These two ratios, which correspond the photon response compensation coefficients, are functions of the incident radiation energy $E_\gamma$. The first task is to compare the values for $Q_{B/A}$ and $Q_{B/C}$ experimentally obtained to the ones calculated by Monte Carlo calculations.

The simulation describes as finely as possible the real samples by perfect cylinders with $h = 8$ mm height, $D = 17.5$ mm diameter, and respective densities $\rho_A = 1.1\ \text{g.cm}^{-3}$, $\rho_B = 1.2\ \text{g.cm}^{-3}$, $\rho_C = 1.1\ \text{g.cm}^{-3}$, using the MCNPX2.7 benz.01t material card to account for the styrene structure of the matrices. The modeled compositions read as follows:

- A: 85.0 wt% carbon, 7.7 wt% hydrogen, 7.1 wt% oxygen, 0.2 wt% nitrogen;
- B: 83.3 wt% carbon, 7.6 wt% hydrogen, 6.9 wt% oxygen, 0.2 wt% nitrogen and 2 wt% gadolinium;
- C: 84.6 wt% carbon, 7.1 wt% hydrogen, 6.2 wt% oxygen, 1.3 wt% nitrogen and 0.8 wt% bismuth.

Coefficients $Q_{B/A}$ and $Q_{B/C}$ are calculated by simulation using the deposition pulse height tally 8 of the MCNPX2.7 code for a set of photon single energy rays $E_\gamma$. We then experimentally compute these coefficient values from the energy spectra acquired as described in the previous paragraph with the three photon radiation sources we can approximate as single-energy: Am-241 ($E_{\gamma,^{241}\text{Am}} = 59\ \text{keV}$), Co-57 ($E_{\gamma,^{57}\text{Co}} = 122\ \text{keV}$) and Cs-137 ($E_{\gamma,^{137}\text{Cs}} = 662\ \text{keV}$). The Na-22 source used for calibration in the previous subsection is excluded since it cannot be approximated as a single-energy source, but rather as a two-peak emitter.

As illustrated on Fig. 4, Fig. 5 and Fig. 6 respectively for counts registered over the full energy spectra, $F_1$ and $F_2$, for B and C used in compensation, on Fig. 7, Fig. 8 and Fig. 9 respectively for counts registered over the full energy spectra, $F_1$ and $F_2$, for B and A used in compensation, the experimental values for the compensation coefficients match the simulation predictions as far as orders of magnitude and tendencies are concerned. Simulated values all converge toward $1.09 \pm 0.02$ from incident energies superior to 200 keV, as well as experimental points obtained with Cs-137 irradiation, which equals the ratio of densities $\frac{\rho_B}{\rho_C} = \frac{\rho_B}{\rho_A} = 1.09$. This is explained by the fact that, above 200 keV, the interactions inside the scintillators are dominated by Compton effects, whose probability is mainly dependent on the density of the propagation medium. On the contrary, below a threshold comprised between 200 and 300 keV, photoelectric effects are prominent, which strongly depend on the effective atomic number of the propagation medium and the incident energy $E_\gamma$. This property explains the higher discrepancy in gamma-ray sensitivity at low energy between the different samples. However, in accordance with simulation results, the difference between the experimental compensation coefficients at 59 keV and 662 keV is reduced when replacing the compensating scintillator A by C (as an example, for countings over $F_1$, $Q_{B/A}(59\ \text{keV}) - Q_{B/A}(662\ \text{keV}) = 11.8$ while $Q_{B/C}(59\ \text{keV}) - Q_{B/C}(662\ \text{keV}) = 3.2$), as the loading in bismuth element brings the effective atomic number of C closer to the one of B. It follows that, as a practical compensation requires the smallest possible dispersion of the compensation coefficient values, further work will solely be oriented toward an optimal loading of the compensating scintillator by heavy atoms such as bismuth.

A real-life photon radiation background may be modeled by a linear combination of single energy rays. As the hypothesis test for neutron detection should be calibrated to operate in the most versatile photon backgrounds, the conceiver needs as many degrees of freedom as possible for the study of the dependence of $Q_{B/C}$ with the incident energy distribution. The limited number of sources practically available in the laboratory and the conformity between simulation and experiment results thus lead to use simulation outputs for further calibration of the detection scheme, as it will be presented in the next paragraph.

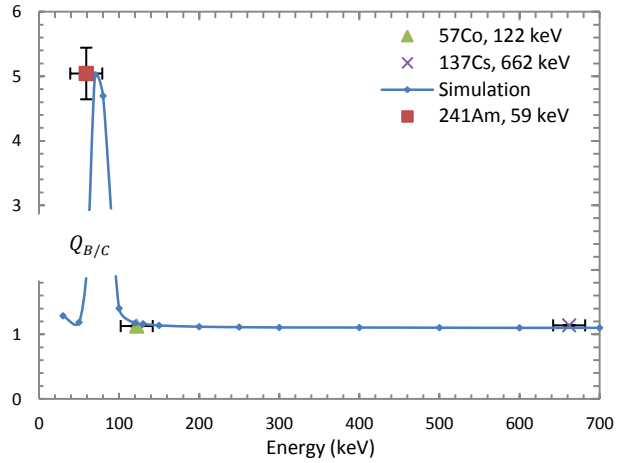


Fig. 4. Photon response compensation coefficient $Q_{B/C}$ as a function of energy for full spectra countings.

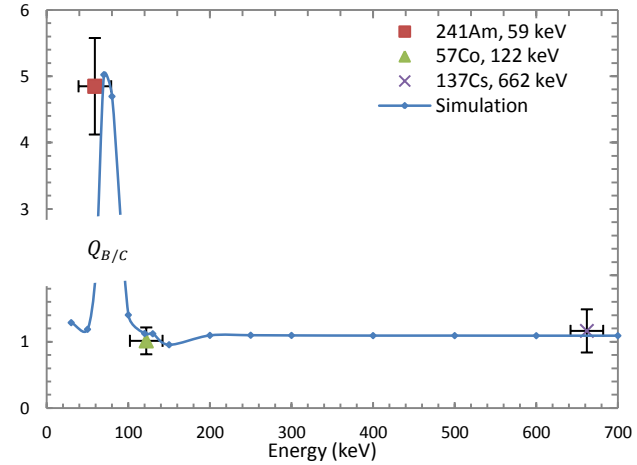


Fig. 5. Photon response compensation coefficient $Q_{B/C}$ as a function of energy for countings over $F_1 = [0; 100\ \text{keV}]$.

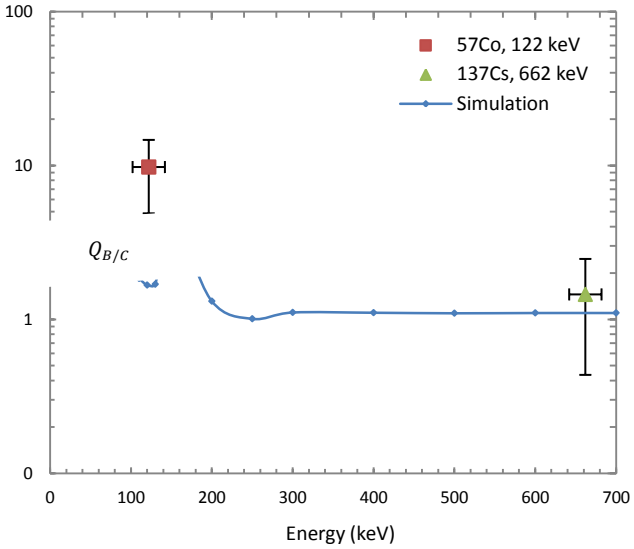


Fig. 6. Photon response compensation coefficient $Q_{B/C}$ as a function of energy for countings over $F_2 = [100\ \text{keV}; 200\ \text{keV}]$.

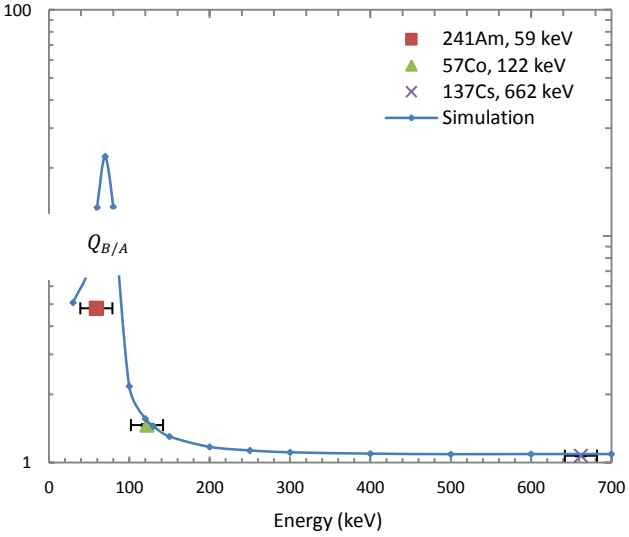


Fig. 7. Photon response compensation coefficient $Q_{B/A}$ as a function of energy for full spectra countings.

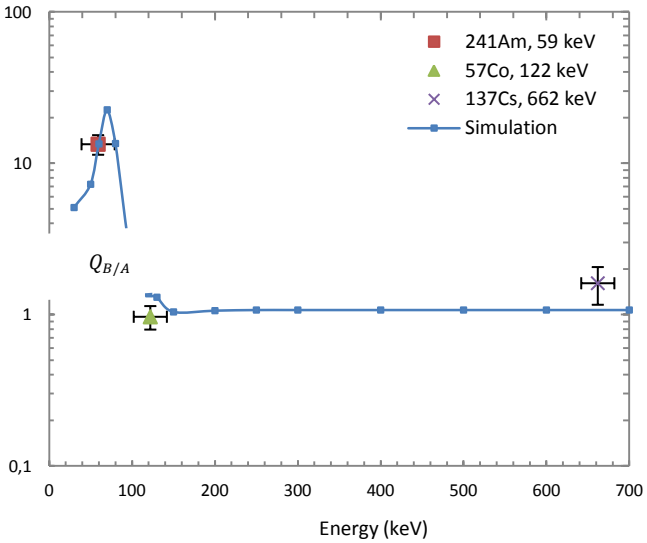


Fig. 8. Photon response compensation coefficient $Q_{B/A}$ as a function of energy for countings over $F_1 = [0; 100\ \text{keV}]$.

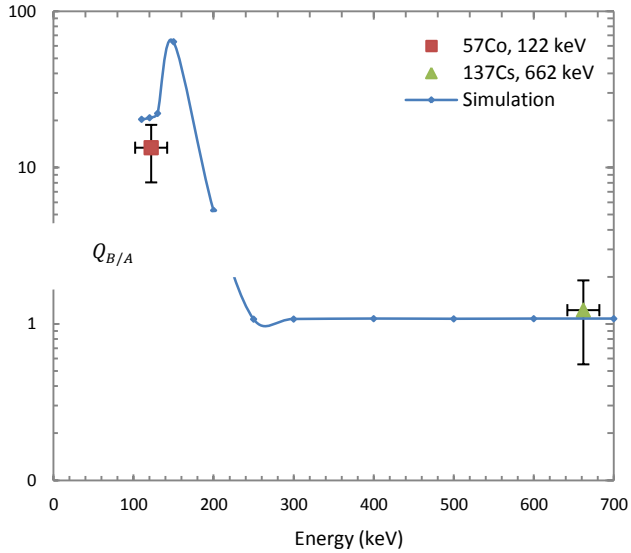


Fig. 9. Photon response compensation coefficient $Q_{B/A}$ as a function of energy for countings over $F_2 = [100\ \text{keV}; 200\ \text{keV}]$.

### *D. Estimation of the photon response compensation coefficient for neutron detection without a priori on the background energy distribution*

In order to compute the values and associated standard deviations for the setting of the compensation coefficient when no *a priori* is available on the photon background energy distribution, this background is simulated with MCNPX code in the form of an isotropic emission spherical source at a distance $d = 10$ cm of the scintillator and whose energy is varied by discrete steps $E_\gamma$ = {30 keV ; 50 keV ; 80 keV ; 100 keV ; 130 keV ; 150 keV ; 200 keV ; 300 keV ; 500 keV ; 1000 keV ; 1500 keV ; 2000 keV} for counting comparisons over the full spectra and $F_1$, and $E_\gamma$ = {130 keV ; 150 keV ; 200 keV ; 300 keV ; 500 keV ; 1000 keV ; 1500 keV ; 2000 keV} over $F_2$. A preliminary run of simulations has enabled us to establish that for small-volume samples, anisotropy effects are negligible when compared with the compensation coefficient dependence on the incident photon energy, which justifies the choice of a spherical geometry source for our simulation. In the absence of *a priori*, a uniform distribution law is postulated between the energy ray. If we label $N_\gamma$ the number of simulated single-energy ray, $E_{\gamma,i}$ for $i$ varying between 1 and $N_\gamma$ each of the energy ray, and $\Delta E_{\gamma,i} = E_{\gamma,i} - E_{\gamma,i-1}$ the weighting coefficient associated with every energy ray under an uniform law hypothesis (by construction, $\Delta E_{\gamma,1} = 0$), the expectation $\bar{Q}$ and the standard deviation $\sigma_{E_\gamma}(\bar{Q})$ associated with the compensation coefficient are estimated according to Eq. (4) and (5) respectively:

$$\bar{Q} = \frac{\sum_{i=2}^{N_\gamma} Q(E_{\gamma,i}) \cdot \Delta E_{\gamma,i}}{\sum_{i=2}^{N_\gamma} \Delta E_{\gamma,i}} \tag{4}$$

$$\sigma_{E_\gamma}(\bar{Q}) = \sqrt{\frac{\sum_{i=2}^{N_\gamma} \left(Q(E_{\gamma,i}) - \bar{Q}\right)^2 \cdot \Delta E_{\gamma,i}}{\sum_{i=2}^{N_\gamma} \Delta E_{\gamma,i}}} \tag{5}$$

The parameters for the photon response compensation obtained by treatment of the simulation results are presented in Table II for counting operations performed over the three considered energy ranges.

TABLE II. EXPECTED COMPENSATION COEFFICIENTS $\bar{Q}$ AND ASSOCIATED DISPERSION STANDARD DEVIATIONS FOR COUNTINGS OVER THE FULL ENERGY SPECTRA AND ENERGY WINDOWS $F_1$ AND $F_2$

| Parameter | Full spectrum | $F_1$ | $F_2$ |
|---|---|---|---|
| $\bar{Q}$ | 1.16 | 1.12 | 1.14 |
| $\sigma_{E_\gamma}(\bar{Q})$ | 0.48 | 0.49 | 0.42 |

One may note that the convergence values (above 200 keV) for this coefficient in the simulation results presented in paragraph *IV.C.*, respectively 1.10, 1.09 and 1.10 over the full spectra, $F_1$ and $F_2$, are within $\bar{Q} \pm 0.1\sigma_{E_\gamma}(\bar{Q})$ over each of the three counting ranges.

### *E. Estimation of the photon response compensation coefficient for neutron detection with* a priori *on the background energy distribution*

Reusing the notations from the previous paragraph, if an *a priori* is available on the energy distribution of the background radioactivity to be compensated, a coefficient $T(E_{\gamma,i})$ may be associated to every single energy ray $E_{\gamma,i}$ used in the calculation, this coefficient modeling the relative intensity of the said ray in the background. Multiplying the distribution $T(E_{\gamma,.})$ with the entire $Q(E_{\gamma,.})$ spectrum, a value $\bar{\bar{Q}}$ of the compensation coefficient taking into account *a priori* knowledge of the radioactive background is calculated as

$$\bar{\bar{Q}} = \frac{\sum_{i=2}^{N_\gamma} Q(E_{\gamma,i}) \cdot T(E_{\gamma,i}) \cdot \Delta E_{\gamma,i}}{\sum_{i=2}^{N_\gamma} \Delta E_{\gamma,i}} \quad (6)$$

### *F. Estimation of the fast neutron response compensation coefficient*

A fast neutron background is simulated using the MCNPX code in the form of an isotropic emission spherical source at a distance $d = 10$ cm of the scintillators B and C. A typical energy for a fast neutron incident on the sensor may be deduced from the spontaneous fission spectrum of Cf-252. This spectrum is described by a Watt distribution, which associates *via* a set of parameters $(C, a, b)$ a fission neutron energy $E_n$ to an emission probability density $(E_n)$ :

$$n(E_n) = C \exp\left(-\frac{E_n}{a}\right) \sinh\left(\sqrt{bE_n}\right) \quad (7)$$

where $C$ is a normalization constant. The parameters $(a, b)$ which characterize the emission spectrum of a Cf -252 source are tabulated [23]: $a = 1.025$ MeV; $b = 2.926$ MeV$^{-1}$. From the distribution, it is possible to extract the expectation for the energy of a spontaneous fission neutron:

$$\widehat{E_n} = \frac{a(ab+6)}{4} = 2.13 \text{ MeV} \quad (8)$$

The fast neutron response compensation coefficient $Q_{B/C}$ is calculated for countings over the full spectra, $F_1 = [0; 100 \text{ keV}]$ and $F_2 = [100 \text{ keV}; 200 \text{ keV}]$ using the deposition pulse height tally 8 of the MCNPX2.7 code, complemented by the deposition pulse height tally 6 and the Pulse Height Light (PHL) option for the computation of proton recoil spectra, which is subsequently corrected in order to take into account the quenching effect and derive a deposited energy $E_n$ expressed in electron-equivalent MeV (MeVee) following [23]

$$E_h \text{ (MeVee)} = 0.034E_h^2 \text{ (MeV)} + 0.125\, E_h\text{(MeV)} \quad (9)$$

TABLE III. COMPENSATION COEFFICIENTS $Q_{B/C}$ FOR COUNTINGS OVER THE FULL ENERGY SPECTRA AND ENERGY WINDOWS $F_1$ AND $F_2$

| Source distribution | Full spectrum | $F_1$ | $F_2$ |
|---|---|---|---|
| $\widehat{E_n}$ | 1.15 | 1.17 | 1.11 |
| $n(E_n)$ | 1.15 | 1.08 | 1.18 |

The value for the fast neutron compensation coefficient $Q_{B/C}$ admits a straightforward physical interpretation. Fast neutron interaction with the propagation medium is dominated by elastic diffusions and the subsequent energy deposition by proton recoil ionization of the medium. Ionization from recoil proton after fission spectrum attenuation is proportional to the number of hydrogen atoms inside the propagation medium, which is proportional itself to the product of weight proportion of hydrogen atoms and density of the medium. Now, the gadolinium-loaded scintillator B and the bismuth-loaded scintillator C have respectively $\%\text{wt}_{H,B} = 7.6$ wt% and $\%\text{wt}_{H,C} = 7.1$ wt% hydrogen mass proportion, and the ratio $\frac{wt\%_{H,B} \cdot \rho_B}{wt\%_{H,C} \cdot \rho_C} = 1.17$. All values presented in Table III are compatible with this expectation within an 8 % relative error. One may also note that both the theoretical expectation and the result of simulation are within $\bar{Q} \pm 0.1\sigma_{E_\gamma}(\bar{Q})$ over each of the three counting ranges, with the notations introduced in paragraph *IV.D.*, meaning that the compensation of a spontaneous fission spectrum inducing proton recoil in both scintillators may be performed with the same parameters as the compensation of a photon background above 200 keV.

## V. SCALING OF THE TWO-SENSOR SYSTEM

### *A. Isolation of the detection and compensation channels*

A practical implementation, based on both the detection scintillator B and the compensation scintillator C, of a neutron counting system requires the isolation of the measurement channels. In the configuration of adjacent scintillators, this isolation is ensured by introducing a thickness of attenuating material between the sensors. Due to its high atomic number $(Z = 82)$ and its high density ($\rho = 11.35$ g.cm$^{-3}$), lead is an excellent candidate for the attenuation of photon radiation. Literature reports a half attenuation length $l_{1/2} = 0.7$ mm for $E_\gamma \leq 200$ keV and $l_{1/2} = 0.9$ cm for $E_\gamma = 1$ MeV. Now Fig. 1 shows that the value of 1 MeV represents a maximum for a significant energy deposition inside small-volume scintillators.

As a consequence, the scaling of the attenuator will be performed in accordance with the attenuation at $E_\gamma = 1$ MeV.

No constraint being formulated at this stage about the occupation and portability of the device, the lead thickness is scaled to ensure a 97.5 % attenuation of a 1 MeV photon radiation, i.e. $l_{1/40}(1\text{ MeV}) = 5.3 \cdot l_{1/2}\ (1\text{ MeV}) = 4.8$ cm.

### *B. Cross-talk over thermal neutron capture signature*

The core issue of channel isolation lies within the limitation of the number of prompt gamma-rays generated in the detection scintillator B after thermal neutron capture and interacting inside the compensation scintillator C. Using once again the source term representing the electron and photon signature of an average gadolinium de-excitation after capture inside B, the ratio of energy deposition rates of this source term inside B and C is estimated by Monte Carlo simulation over the full spectra and energy windows $F_1 = [0; 100\text{ keV}]$ and $F_2 = [100\text{ keV}; 200\text{ keV}]$. Scintillators are simulated side-by-side and separated by a lead block of height $h = 8$ mm and thickness $x = 4.8$ cm. The source term emission is isotropic and homogeny inside B. Energy deposition yields inside B and C, respectively noted $\tau_{D,B}$ et $\tau_{D,C}$, are evaluated using the MCNPX2.7 deposition pulse height tally 8. The values for the ratio $Q_{D,B/C} = \frac{\tau_{D,B}}{\tau_{D,C}}$, of these yields for countings over the energy ranges of interest are reported in Table IV.

TABLE IV. RATIOS OF ENERGY DEPOSITION YIELDS OF THE DETECTION SOURCE TERM INSIDE B AND C

| | Full spectrum | $F_1$ | $F_2$ |
|---|---|---|---|
| $Q_{D,B/C}$ | $6.10^4$ | $1.10^4$ | $9.10^3$ |

It follows that, for a suitably scaled insulator block, cross-talk over the detection signal is negligible over all counting ranges of interest.

### *C. Cross-talk over recoil electrons and shielding effect*

It is additionally necessary to verify that the estimation of compensation coefficients for photon and fast neutron radioactivity is not biased when the sensor's are assembled and isolated. For this purpose, spherical isotropic radiation backgrounds are simulated at a distance $d = 10$ cm of the barycenter of the assembled system (*i.e.* the center of the lead block). All tests confirm the absence of significant bias within the uncertainties derived for the compensation coefficients in paragraph *IV.D.*, meaning that multiple diffusions of incident photons and fast neutrons in the three physical parts of the system (detection scintillator, attenuator, compensation scintillator) have negligible impact on the measurement, as well as recoil electrons generated in one scintillator and crossing the attenuator to interact within the second scintillator. In other words, there is no significant shielding of any of the physical parts on the thermal neutron detector resulting of the compensation of B by C, nor is there any significant cross-talk between measurement channels under background radiation. As an illustration, Table V shows a comparison between compensation coefficients computed using the MCNPX2.7 deposition pulse height tally 8 in presence of a $E_\gamma = 662$ keV Cs-137 ray for the scintillators being simulated separately as described in Part *IV*, and assembled with lead attenuator as introduced in paragraph *V.B.* The same comparison was drawn in Table VI in presence of the Watt spectrum $n(E_n)$ describing an average spontaneous fission of Cf-252, using the deposition pulse height tally 6 and the PHL option for the computation.

TABLE V. COMPENSATION COEFFICIENTS $Q_{B/C}$ FOR SENSORS SIMULATED SEPARATELY AND ASSEMBLED IN PRESENCE OF $E_\gamma = 662$ KEV GAMMA-RAY

| Coefficient $Q_{B/C}$ | Full spectrum | $F_1$ | $F_2$ |
|---|---|---|---|
| Separately | 1.10 | 1.09 | 1.10 |
| Assembled | 1.10 | 1.10 | 1.10 |

TABLE VI. COMPENSATION COEFFICIENTS $Q_{B/C}$ FOR SENSORS SIMULATED SEPARATELY AND ASSEMBLED IN PRESENCE OF $n(E_n)$ NEUTRON SPECTRUM

| Coefficient $Q_{B/C}$ | Full spectrum | $F_1$ | $F_2$ |
|---|---|---|---|
| Separately | 1.15 | 1.08 | 1.18 |
| Assembled | 1.16 | 1.11 | 1.13 |

The values of $Q_{B/C}$ for the sensors being simulated separately or assembled are consistent within 4 % relative error. Over all counting ranges, they are moreover compatible by $\pm 0.1\sigma_{E_\gamma}(\bar{Q})$ with the expectation $\bar{Q}$ calculated in paragraph *IV.D.* for an uniformly distributed photon background.

Because the relative responses of the sensors may be studied indifferently together with lead or separately, we have chosen to assess the neutron sensitivity of the detection scheme in varying backgrounds by successive and separate countings on B and C, in order to avoid biases due to the acquisition and measurement chain.

## VI. NONLINEAR SMOOTHING AND HYPOTHESIS TEST FOR NEUTRON DETECTION AND COUNTING

This section presents the simulation of online treatment of the countings on the detection and compensation channels as performed in the software of unit (9) described in Fig. 2. From the counts $N_B$ and $N_C$, integrated over a $T = 180$ s temporal window (empirically identified as sufficient to achieve precise and stable count rate estimates), the expected count rates on channel 1 (B) and channel 2 (C), respectively noted $\lambda_B$ and $\lambda_C$, are computed as

$$\lambda_B = \frac{N_B}{T} \tag{10}$$

$$\lambda_C = \frac{N_C}{T} \tag{11}$$

In order to simulate a realistic counting measurement, pulse frames $\boldsymbol{N_B^t}$ and $\boldsymbol{N_C^t}$ are created with a temporal step $\Delta t = 0.1$ s (compatible with real-time monitoring of the raw signals) on channels 1 and 2 by the means of the "Poissrnd" $\wp$ Matlab function, which generates random numbers $N_B^t$ and $N_C^t$, composing the said vectors, following a Poisson-type probability distribution, respectively parameterized by $\lambda_B$ and $\lambda_C$ as made explicit in:

$$\forall\, t \in [0\,;180], N_B^t \sim \wp(\lambda_B \cdot \Delta t) \tag{12}$$

$$\forall\, t \in [0\,;180], N_C^t \sim \wp(\lambda_C \cdot \Delta t) \tag{13}$$

With such a small temporal step, the raw variance of the signals registered every $\Delta t$ on channels 1 and 2 may tend to overcome the amplitude of the signal itself, especially at low count rates which are expected for small-volume sensors. Yet neutron detection occurs when the pondered difference between both channels is significantly superior to the level of statistic fluctuations. For the test to be sensitive, the said level of fluctuations should therefore be as drastically reduced as possible, which is why the hypothesis test should be preceded by a smoothing operation of the signals registered on channels 1 and 2.

### *A. Nonlinear smoothing of counting signals*

In order to maintain a satisfactory level of count rate stability while allowing for a short response time variation monitoring of the radioactivity measured on channels 1 and 2, the authors have implemented on both channels a nonlinear smoother for online nuclear counting measurements. The principle of the smoothing operation is based on the adaptation of a retained window of count values for the estimation of the activity in accordance with the detection or not-detection of an abrupt change in the underlying Poisson statistics of the signal. The detection or not-detection is respectively determined by the acceptance or rejection of a law hypothesis. The smoothing operation whose principle is detailed below has been named Centered Significance Test and labeled $CST$ [24].

The algorithm followed by the $CST$ filter may be schematically divided into four steps, illustrated on the data acquired on channel 1:

a. *Reading and data storage*. During every elementary time interval $\Delta t$, pulses are counted. At the end $t$ of a given counting interval, the count number $N_{B,1}^{t}$ is recorded at the front of a memory buffer containing $M$ slots. Before any additional acquisition, all stored values are shifted to the right as presented in:

$$\forall t \in [0.1; T], \forall j \in [2; M], N_{B,j}^{t} = N_{B,j-1}^{t-\Delta t} \quad (14)$$

b. *Calculation of an estimate vector*. A vector $\widehat{\boldsymbol{\Lambda}_{\boldsymbol{B}}^{\boldsymbol{t}}}$ storing count rate estimates $\hat{\lambda}_{B,i}^{t}$ computed over several sample windows of size $i$, each associated with a response time and precision performance, is built as described in Eq. (15). The scalar $l^t$ represents at every time $t$ the maximal sample number retained for the estimation. The fundamental operation of the filter consists in determining, for a given $t$, the value of $i$ allowing the highest precision of the estimate over the shortest number of samples (to preserve as much useful temporal information as possible).

$$\forall t \in [0.1; T], \forall i \in [1; l^t],\ \hat{\lambda}_{B,i}^{t} = \frac{1}{i}\sum_{j=1}^{i} N_{B,j}^{t} \quad (15)$$

c. *Decision test*. The true count rate value is defined as a function of the acquisition time $t$ under the form $\lambda_B^t$. The detection test for an abrupt change in radioactivity takes the form of a classical hypothesis test with a null hypothesis $\mathbf{H_0}$ representing the absence of any change in activity detected and the non-null hypothesis $\mathbf{H_1}$ representing a change in activity detected. If $\gamma_0$ is the initial count rate level, $\gamma_1$ a potential different signal level after a change in radioactivity, and $\omega^t$ the sample label at which such a change would have been detected, both hypotheses read

$$\mathbf{H_0}: \forall i \in [0;\ l^t], \lambda_B^{t-i\Delta t} = \gamma_0 \quad (16)$$

$$\mathbf{H_1}: \exists \omega^t \in [0;\ l^t] / \forall i \in [0;\ \omega^t], \lambda_B^{t-i\Delta t} = \gamma_0 \quad \forall i \in ]\omega^t;\ l^t], \lambda_B^{t-i\Delta t} = \gamma_1 \quad (17)$$

To determine, at the time $t$, the position $\omega^t$ of a significant detected radioactivity change inside the previously selected integration window $l^t$, every estimate $\hat{\lambda}_{B,i}^{t}$ is compared to the estimate $\hat{\lambda}_{B,l^t}^{t}$. A variation vector $\widehat{\boldsymbol{\Delta\Lambda_B^t}}$ is built, whose components are computed as described in:

$$\forall i \in [1; l^t], \Delta\hat{\lambda}_{B,i}^{t} = \hat{\lambda}_{B,l^t}^{t} - \hat{\lambda}_{B,i}^{t} \quad (18)$$

The variance is calculated as a sum of variances from independent variables under Poisson statistics:

$$\sigma^2\left(\Delta\hat{\lambda}_{B,i}^{t}\right) = \sigma^2\left(\hat{\lambda}_{B,l^t}^{t}\right) + \sigma^2\left(\hat{\lambda}_{B,i}^{t}\right) = \frac{\hat{\lambda}_{B,l^t}^{t}}{l^t} + \frac{\hat{\lambda}_{B,i}^{t}}{i} \quad (19)$$

If $\mathbf{H_0}$ is verified, as the difference of two count rate estimates under the same underlying true rate, the value of $\Delta\hat{\lambda}_{B,i}^{t}$ should be null. On the contrary, any radioactivity change in $\lambda_B^t$, which should lead to rejection of $\mathbf{H_1}$, means a significantly non null $\Delta\hat{\lambda}_{B,i}^{t}$. We introduce $\alpha = P(\mathbf{H_1}|\mathbf{H_0})$ as the probability of wrongful radioactivity change detection and $t_\alpha$ as the coverage factor of the decision test. A distribution $f$ associates a probability of false detection $\alpha$ to every value of $t_\alpha$: $\alpha = f(t_\alpha)$. Eventually, the decision test for the detection of radioactivity change at the acquisition time $t$ reads as follows:

$$\text{If: } \exists i \in [0;\ l^t], \left|\Delta\hat{\lambda}_{B,i}^{t}\right| > t_\alpha \sigma\left(\Delta\hat{\lambda}_{B,i}^{t}\right) \quad (20)$$

Then $\mathbf{H_1}$ is accepted with a confidence level $1-\alpha$.

d. *Adjustment of the estimation window*: In accordance with the result of the decision test, the sample window over which the count rate is estimate is adjusted. In case $\mathbf{H_0}$ is accepted for all slots $i \in [0;\ l^t]$, no abrupt radioactivity change has to be taken into account, and the statistical precision of the estimator may be improved by extending the number of slots allocated to the estimation at the next acquisition step: $l^{t+\Delta t} = l^t + 1$. If, on the contrary, $\mathbf{H_1}$ is accepted for a slot number $\omega^t$, a radioactivity change is detected as significant and the estimation window should be shortened to preserve the temporal information contained in an abrupt variation. The number of slots allocated to the count rate estimation is therefore reduced by $F$ slots, where $F$ equals the number of slots verifying Eq. (20): $l^{t+\Delta t} = l^t - F$. The expectations $\widehat{\lambda_B^t}$, $\widehat{N_B^t} = \widehat{\lambda_B^t} \cdot \Delta t$ and variance $\sigma^2\left(\hat{\lambda}_{B,l^t}^{t}\right) = \frac{\hat{\lambda}_{B,l^{t+\Delta t}}^{t}}{l^{t+\Delta t}}$ are eventually delivered at the output of the filter as respectively, the current count rate and count estimates at the time $t$.

Preliminary studies [25] have established the convergence of the filter outputs with count rates superior to 0.1 cps for an initial buffer size $M$ exceeding 100 samples and described the optimization of the response time versus precision tradeoff as a function of the test parameter $t_\alpha$. On the basis of these results, and given the low volume of the scintillating samples (hence their low radiation sensitivity) the authors have selected the values $M = 1800$ samples (i.e. the entire acquisition time) and $t_\alpha = 1.65$ for the implementation of the *CST* smoother.

### B. Hypothesis test for neutron detection

Let $\widehat{N_B^t}$ and $\widehat{N_C^t}$ be the smoothed counting values exiting the *CST* smoother on channel 1 and 2 respectively. Let additionally $\sigma^2(\widehat{N_B^t})$ and $\sigma^2(\widehat{N_C^t})$ be the reduced variances respectively associated to $\widehat{N_B^t}$ and $\widehat{N_C^t}$ at the output of the smoother, $\bar{Q}$ and $\sigma_{E_\gamma}^2(\bar{Q})$ respectively the average compensation coefficient calculated with no *a priori* on the background and its variance over a uniform energy distribution between 0 and 2 MeV, $\bar{\bar{Q}}$ the compensation coefficient calculated with *a priori* knowledge of the background distribution. These notations are summarized in:

$$[\widehat{N_B^t}\,;\,\sigma^2(\widehat{N_B^t})] = CST(N_B^t) \quad (21)$$

$$[\widehat{N_C^t}\,;\,\sigma^2(\widehat{N_C^t})] = CST(N_C^t) \quad (22)$$

The estimated counting signal attributed to neutrons at the time $t$ is labeled $\widehat{N_n^t}$. The neutron detection and counting operation is the result of a hypothesis test parameterized by a coverage factor $K$. Similarly to the decision test in the nonlinear filter described *supra*, a distribution $g$ associates a probability of false neutron detection $K$ to every value of $t_K$: $K = g(t_K)$. Depending on whether an *a priori* is available (Eq. (23)) on the radioactive background or not (Eq. (24)), the detection test and subsequent neutron counting read:

If:

$$\widehat{N_B^t} - \bar{Q}\cdot\widehat{N_C^t} > t_K\cdot\sqrt{\sigma^2(\widehat{N_B^t}) + \bar{Q}^2\cdot\sigma^2(\widehat{N_C^t}) + \sigma_{E_\gamma}(\bar{Q})^2\cdot\widehat{N_C^t}^2}$$

Then: $\widehat{N_n^t} = \widehat{N_B^t} - \bar{Q}\cdot\widehat{N_C^t}$

Else: $\widehat{N_n^t} = 0$ (23)

If:

$$\widehat{N_B^t} - \bar{\bar{Q}}\cdot\widehat{N_C^t} > t_K\cdot\sqrt{\sigma^2(\widehat{N_B^t}) + \bar{\bar{Q}}^2\cdot\sigma^2(\widehat{N_C^t})}$$

Then: $\widehat{N_n^t} = \widehat{N_B^t} - \bar{\bar{Q}}\cdot\widehat{N_C^t}$

Else: $\widehat{N_n^t} = 0$ (24)

The values $\widehat{N_n^t}$ are stored in a temporal vector $\widehat{\boldsymbol{N_n^t}}$. By dividing the resulting counts obtained every $\Delta t$ by the temporal step, an estimate for instantaneous count rate vector $\widehat{\boldsymbol{\lambda_n^t}}$ is obtained:

$$\widehat{\boldsymbol{\lambda_n^t}} = \frac{\widehat{\boldsymbol{N_n^t}}}{\Delta t} \quad (25)$$

The output of the neutron counting measurement is provided by the empirical temporal mean of the instantaneous count rate vector, labeled $\widehat{\lambda_n}$, around which an empirical variance $\sigma^2(\widehat{\lambda_n})$ is calculated to represent the dispersion of the actual instantaneous count rates around the mean.

## VII. Experimental results

Four counting measurements are performed over $T = 180$ s with B (channel 1) and C (channel 2):

- measurement of the background radiation activity in the experiment room, labeled *background* measurement;
- measurement in presence of a *Cs-137* source of activity $A_{^{137}\mathrm{Cs}} = 178$ kBq positioned at a distance $d = 10$ cm of the scintillator surface along the symmetry axis of the scintillator;
- measurement in presence of a *Cf-252* source of activity $A_{^{252}\mathrm{Cf}} = 1.2$ MBq with 10 cm High Density Polyethylene (HDPE) moderator in between;
- measurement in presence of an *Am-241* source of activity $A_{^{241}\mathrm{Am}} = 1$ kBq in contact with the scintillator.

The net average count rates $\lambda_B$ and $\lambda_C$ obtained on each channel over the full spectra and energy windows $F_1$ and $F_2$ are listed in Table VII.

TABLE VII. AVERAGE COUNT RATES IN COUNT PER SECOND (CPS) WITH B AND C SCINTILLATORS OVER THE ENERGY RANGES OF INTEREST

| Energy range \ Radioactive source | Background | Cs-137 (10 cm) | Cf-252 (+ 10 cm HDPE) | Am-241 (in contact) |
|---|---|---|---|---|
| **Full spectrum** | B : 2.3<br>C : 0.8 | B : 308.5<br>C : 271.0 | B : 83.6<br>C : 48.8 | B : 8.5<br>C : 1.8 |
| $F_1$ | B : 2.0<br>C : 0.5 | B : 127.9<br>C : 110.1 | B : 48.7<br>C : 26.3 | B : 7.1<br>C : 1.5 |
| $F_2$ | B : 0.1<br>C : 0.0 | B : 59.5<br>C : 41.1 | B : 10.1<br>C : 4.5 | B : 0.4<br>C : 0.2 |

### A. Estimation of neutron sensitivity with Cf-252 source in the absence of radioactive background

A sealed Cf-252 source is both a neutron and photon radiation emitter. Neutron emission is described by a Watt spectrum parameterized as stated in paragraph *IV.F*. This emission is associated to spontaneous fissions [26], which account for 3.09 % of a Cf-252 source activity. The mean number of neutrons emitted per fission $\nu_n = 3.77$ n.f$^{-1}$. This neutron emission is accompanied by a photon background, composed of prompt and delayed gamma-rays (X- and gamma-rays associated to alpha disintegrations are neglected due to low emission probabilities for energies superior to 20 keV). The resultant background distribution is modeled [27] by a piecewise defined function $p$ of photon energy $E_\gamma$, so that $p(E_\gamma) = Dc(E_\gamma)$, where $D$ is a normalization constant and $c$ reads

$$c(E_\gamma) = \begin{cases} 6.6 + e^{-1.1E_\gamma}, 20\text{ keV} < E_\gamma < 500\text{ keV} \\ 20.2e^{-1.78E_\gamma} + e^{-1.1E_\gamma}, 500\text{ keV} \le E_\gamma < 1.4\text{ MeV} \\ 7.2e^{-1.09E_\gamma} + e^{-1.1E_\gamma}, 1.4\text{ MeV} \le E_\gamma < 10.4\text{ MeV} \end{cases} \quad (26)$$

The values reported in literature for the mean number $\nu_\gamma$ of gamma-rays produced by spontaneous fission vary between 7 and 10 [28]; we retain the value $\nu_\gamma = 7.98$ proposed by Valentine [29]. The coefficient $Q_{B/C,\gamma}$ for moderated Cf-252 gamma-ray background compensation and $Q_{B/C,n}$ for moderated Cf-252 fission spectrum background compensation are calculated by simulation of scintillators B and C and the point source described by Eq. (6) and (26), with an additional moderator between the source and the sensors, modeled by a perfect cylinder with the same symmetry axis as B and C, $h = 10$ cm height and $d = 5.7$ cm diameter, composed of one third of carbon atoms and two thirds of hydrogen atoms, with 0.95 g.cm$^{-3}$ density and using the MCNPX2.7 poly.01t material card to account for thermal neutron scattering inside polyethylene. The resulting $Q_{B/C}$ compensation coefficient for Cf-252 photon and fast neutron radioactivity reads

$$Q_{B/C} = \frac{\nu_n \cdot Q_{B/C,n} + \nu_\gamma \cdot Q_{B/C,\gamma}}{\nu_n + \nu_\gamma} \quad (27)$$

The values for this coefficient estimated for countings over the full spectra and energy ranges are presented in Table VIII.

TABLE VIII. COMPENSATION COEFFICIENTS $Q_{B/C}$ FOR MODERATED CF-252 BACKGROUND OBTAINED BY SIMULATION

| | Full spectrum | $F_1$ | $F_2$ |
|---|---|---|---|
| Coefficient $Q_{B/C}$ | 1.20 | 1.07 | 1.14 |

The values for the compensation coefficient are within $\bar{Q} \pm 0.1\sigma_{E_\gamma}(\bar{Q})$ (with the notations defined in paragraph *IV.D.*) over the three ranges, so that the counting operation may be parameterized by the couple of parameters $\{\bar{Q}; \sigma_{E_\gamma}(\bar{Q})\}$ inside the hypothesis test described by Eq. (23). This result means that, according to simulation, the photon and fast neutron radioactivity of the moderated Cf-252 source is similar, from the prospective of compensation, to the activity of a photon emissive source above 200 keV, such as Cs-137. Such similarity is corroborated by the equivalence in energy distributions from both radiations as induced in the thermal neutron-insensitive scintillator C over the energy windows of interest: according to Table VII, for instance, 64 % of the counts induced in C by the moderated Cf-252 source lie below 200 keV, while, for the same scintillator, 66 % of the counts induced by the Cs-137 source lie below 200 keV.

The value of the coverage factor in the hypothesis test (Eq. (23)) for neutron counting $t_K$ governs the thermal neutron sensitivity $S_n$ versus false detection probability $K$ compromise. The distributions $K = g(t_K)$ for the couple of parameters $\{\bar{Q}; \sigma_{E_\gamma}(\bar{Q})\}$ reported in Table II corresponding to countings over full spectra, $F_1 = [0; 100\text{ keV}]$ and $F_2 = [100\text{ keV}; 200\text{ keV}]$, are presented in Fig. 10. As these values depend on the order of magnitude of the counts registered, we chose to base the setting of the coverage factor $t_K$ on the lowest non-null activity on one channel presented in Table VII, equaling 0.1 cps (i.e. 18 cp over $T = 180$ s integration time). This activity is responsible for the slowest decreasing distribution $K = g(t_K)$, and therefore the level of confidence $1 - K$ of the test derived from this distribution sets a lower limit to the ones obtained with superior count rates registered on both channels.

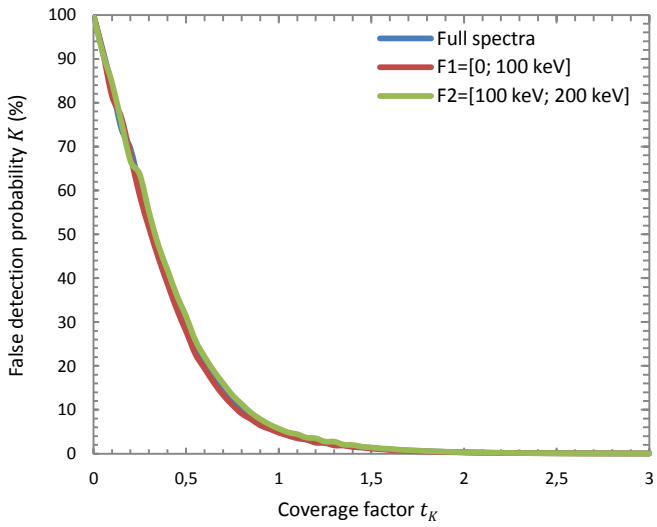


Fig. 10. Distribution $K = g(t_K)$ evaluated for $\widehat{N_C^t} = 18$ cp, $\widehat{N_B^t} = \bar{Q} \cdot \widehat{N_C^t}$.

On the basis on the three distributions superimposed in Fig. 10, the coverage factor was set $t_K = 3$ associated to a confidence level $1 - K = (99.99 \pm 0.01)$ %.

The spectra measured with scintillators B and C separately and successively under moderated Cf-252 irradiation are reproduced together in Fig. 11. The discrepancy between both spectra is manifest up to 200 keV, as predicted from simulation output presented in Fig. 1, hence validating the choice of selective countings over energy ranges below 200 keV. The evolution of the displayed neutron count rate $\widehat{\lambda_n} \pm \sigma(\widehat{\lambda_n})$ as a function of the coverage factor $t_K$ parameterizing hypothesis test (19) is presented in Fig. 12, 13 and 14 for countings over the full spectra, $F_1 = [0; 100\text{ keV}]$ and $F_2 = [100\text{ keV}; 200\text{ keV}]$ respectively. It follows that for a coverage factor $t_K = 3$, the neutron rate reads $\widehat{\lambda_n} = 11.1 \pm 0.2$ cps, $\widehat{\lambda_n} = 4.6 \pm 0.2$ cps and $\widehat{\lambda_n} = 2.8 \pm 0.1$ cps over the full spectra, $F_1$ and $F_2$ respectively.

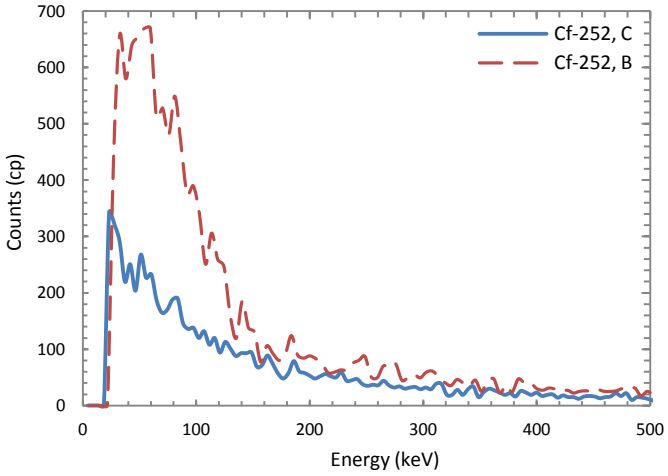


Fig. 11. Amplitude spectra of scintillators B and C in presence of the moderated Cf-252 source.

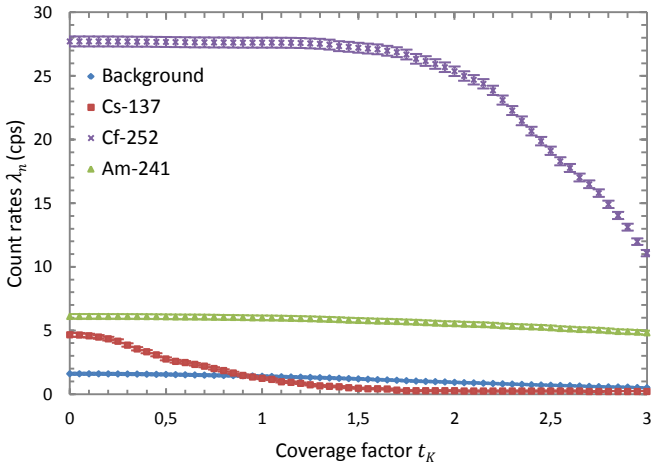


Fig. 12. Count rates $\widehat{\lambda_n}$ and $\widehat{\lambda_{n/\gamma}}$ over full spectra as a function of the coverage factor $t_K$.

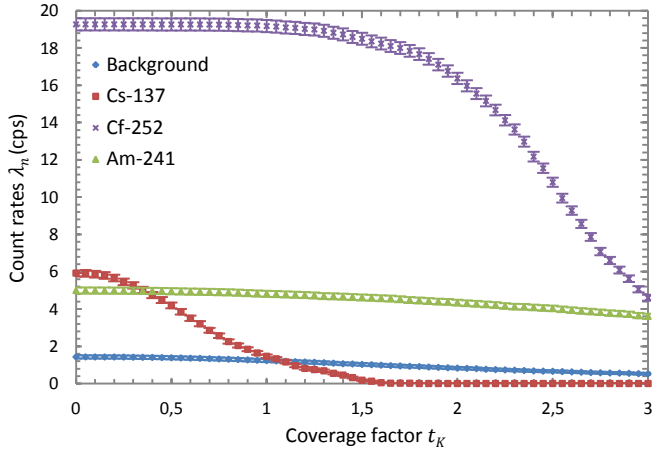


Fig. 13. Count rates $\widehat{\lambda_n}$ and $\widehat{\lambda_{n/\gamma}}$ over $F_1$ as a function of the coverage factor $t_K$.

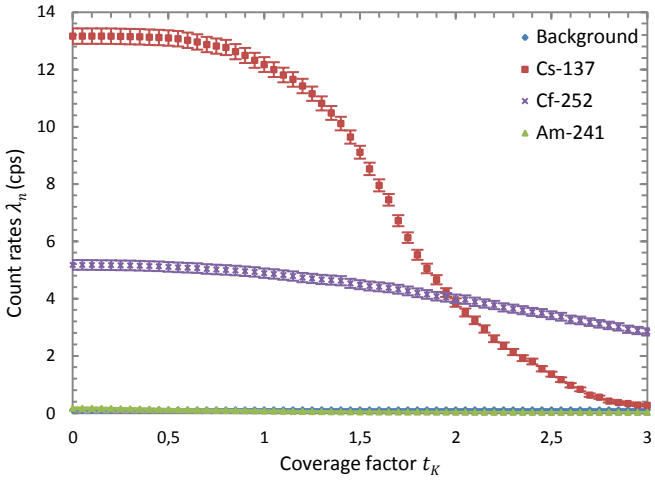


Fig. 14. Count rates $\widehat{\lambda_n}$ and $\widehat{\lambda_{n/\gamma}}$ over $F_2$ as a function of the coverage factor $t_K$.

In order to benchmark the thermal neutron detection scheme based on the physical sensors and numerical parameters we have introduced, with reference He-3 proportional counters, a thermal neutron sensitivity estimate labeled $\widehat{S_n}$ and expressed in count per thermal neutron $n_{th}$ times square centimeter ($\mathrm{c}.n_{th}^{-1}.\mathrm{cm}^2$ or cps/nv) has to be calculated. The spontaneous fission rate the Cf-252 source reads $A_{^{252}\mathrm{Cf},\mathrm{f}} = 0.0309 \cdot A_{^{252}\mathrm{Cf}} = 3.7 \cdot 10^4\ \mathrm{f}.\mathrm{s}^{-1}$ expressed in fission per second, and the fission neutron rate $A_{^{252}\mathrm{Cf},n} = 3.77 \cdot A_{^{252}\mathrm{Cf},\mathrm{f}} = 1.4 \cdot 10^5\ n.\mathrm{s}^{-1}$ expressed in neutron per second. The thermal neutron fluence incident on scintillator B or C at the exit of the HDPE moderator, i.e. the neutron fluence integrated between 1 meV and 50 meV (cadmium absorption cut-off), labeled $\Psi_{n_{th}}$ and expressed in thermal neutron per generated neutron and square centimeter ($n_{th}.n^{-1}.\mathrm{cm}^{-2}$), is evaluated by simulation using the average surface flux tally 2 of the MCNPX2.7 code. The estimate reads $\Psi_{n_{th}} = 2.4 \cdot 10^{-5}\ n_{th}.n^{-1}.\mathrm{cm}^{-2}$, from which an estimate of the thermal neutron flux incident on a sensor, labeled $\Phi_{n_{th}}$ and expressed in thermal neutron per square centimeter and per second ($n_{th}.\mathrm{cm}^{-2}.\mathrm{s}^{-1}$), is derived as $\Phi_{n_{th}} = \Psi_{n_{th}} \cdot A_{^{252}\mathrm{Cf},n} = 3.3\ n_{th}.\mathrm{cm}^{-2}.\mathrm{s}^{-1}$. The thermal neutron sensitivity estimate is calculated as

$$\widehat{S_n} = \frac{\widehat{\lambda_n}}{\Phi_{n_{th}}} \tag{28}$$

equaling $\widehat{S_n} = 3.3 \pm 0.1$ cps/nv, $\widehat{S_n} = 1.4 \pm 0.1$ cps/nv and $\widehat{S_n} = 0.9 \pm 0.1$ cps/nv for countings over full spectra, $F_1$ and $F_2$ respectively. To provide a commercial reference, these estimates are within the same order of magnitude as the thermal neutron sensitivities claimed for VacuTec 70060 type He-3 counters of similar active volume (2.8 $\mathrm{cm}^3$), ranging between 0.6 and 2.0 cps/nv for gas pressure varied between 2 and 10 bars [30].

*B. Influence of radiation background on neutron activity estimation*

Three background measurements, representative of different radiation activities to be compensated in order to display a trustable neutron rate, have been performed following the algorithmic steps described in Section V and the experimental inputs recorded in Table VII.

a. Background measurement

The evolution of the noise count rate $\widehat{\lambda_{n/\gamma}} \pm \sigma\left(\widehat{\lambda_{n/\gamma}}\right)$ in presence of the background radiation of the experiment room is presented in Fig. 12, 13 and 14 as a function of the coverage factor $t_K$ for countings over the full spectra, $F_1$ and $F_2$ respectively. For a parameter $t_K = 3$, the displayed rates read $\widehat{\lambda_{n/\gamma}} = 0.5 \pm 0.1$ cps, $\widehat{\lambda_{n/\gamma}} = 0.5 \pm 0.1$ cps and $\widehat{\lambda_{n/\gamma}} = 0.1 \pm 0.1$ cps, which all lie within $\pm 3\sigma\left(\widehat{\lambda_n}\right)$ for the previously described moderated Cf-252 measurement. This result means that in presence of the natural radiation background of the experiment room, whose gamma dose rate is measured equal to 0.2 µSv.h$^{-1}$ with a commercial Thermo Electron ESM FH 40G-L 10 radiometer, the neutron activity measurement described in paragraph VII.A. is unbiased within three standard deviations. The robustness of the compensation operation over of the background measurement is explained by the fact that the energy distribution of standard natural radioactivity lies in average above 200 keV (between 300 keV and 1 MeV for instance in Medhat et al. [31]), and therefore that the couple of parameters $\{\bar{Q}; \sigma_{E_\gamma}(\bar{Q})\}$ used to set the coverage factor $t_K = 3$ is indeed representative of the background to be corrected. The estimate for the detection limit in a "conventional" environment (dose rate below 0.5 µSv.h$^{-1}$ [32]), labeled $\widehat{DL_n}$ and expressed in thermal neutron flux (nv), is derived from the residual noise rate in the absence of the Cf-252 source as

$$\widehat{DL_n} = \frac{\widehat{\lambda_{n/\gamma}}}{\widehat{S_n}} \tag{29}$$

equaling $\widehat{DL_n} = 0.15 \pm 0.03$ nv, $\widehat{DL_n} = 0.36 \pm 0.07$ nv and $\widehat{DL_n} = 0.11 \pm 0.11$ nv for countings over full spectra, $F_1$ and $F_2$ respectively.

b. Cs-137 source

The evolution of the noise count rate $\widehat{\lambda_{n/\gamma}} \pm \sigma\left(\widehat{\lambda_{n/\gamma}}\right)$ in presence of the Cs-137 source (typically used for neutron detector evaluation as representative of long-lived fission products present in the fuel cycle) is presented in Fig. 12, 13 and 14 as a function of the coverage factor $t_K$ for countings over the full spectra, $F_1$ and $F_2$ respectively. For a parameter $t_K = 3$, the displayed rates read $\widehat{\lambda_{n/\gamma}} = 0.2 \pm 0.03$ cps, $\widehat{\lambda_{n/\gamma}} = 0.01 \pm 0.01$ cps and $\widehat{\lambda_{n/\gamma}} = 0.3 \pm 0.04$ cps, which all lie within $\pm 3\sigma\left(\widehat{\lambda_n}\right)$ for the previously described moderated Cf-252 measurement. This result means that in presence of the Cs-137, whose gamma dose rate is measured equal to 3.2 µSv.h$^{-1}$, the neutron activity measurement described in paragraph VII.A. is unbiased within three standard deviations. The robustness of the compensation operation over a Cs-137 photon background is straightforward from the observations drawn in paragraph *IV.C.*, with compensation coefficients at 662 keV within $\bar{Q} \pm 0.1\sigma_{E_\gamma}(\bar{Q})$. The estimate for the detection limit in this typical a "monitored area" environment (defined by dose rates ranging from 0.5 up to 7.5 µSv.h$^{-1}$) read $\widehat{DL_n} = 0.06 \pm 0.01$ nv, $\widehat{DL_n} = 0.01 \pm 0.01$ nv and $\widehat{DL_n} = 0.33 \pm 0.04$ nv for countings over full spectra, $F_1$ and $F_2$ respectively.

c. Am-241 source

The evolution of the noise count rate $\widehat{\lambda_{n/\gamma}} \pm \sigma\left(\widehat{\lambda_{n/\gamma}}\right)$ in presence of the Am-241 source is presented in Fig. 12, 13 and 14 as a function of the coverage factor $t_K$ for countings over the full spectra, $F_1$ and $F_2$ respectively. Though less usual in neutron detector evaluation, such a background measurement is representative of radiative hot spots, as, for instance, potentially present in glove boxes. Because sealed Am-241 is a photon emitter below 60 keV, the source induces no significant noise rate over energy window $F_2 = [100 \text{ keV}; 200 \text{ keV}]$: $\widehat{\lambda_{n/\gamma}} = 0.02 \pm 0.01$ cps, hence a detection limit $\widehat{DL_n} = 0.01 \pm 0.01$ nv over $F_2$. However, there is no compensation of the Am-241 background for countings over full spectra and $F_1$ at $t_K = 3$, and therefore no possibility to guarantee a robust neutron counting over these ranges. This is due to the fact that the couple of parameters $\{\bar{Q} = 1.16\,; \sigma_{E_\gamma}(\bar{Q}) = 0.48\}$ over full spectra and $\{\bar{Q} = 1.12\,; \sigma_{E_\gamma}(\bar{Q}) = 0.49\}$ over $F_1$ used in the calibration curves of the hypothesis test displayed in Fig. 10 are not representative of the correction of an Am-241 background, with experimentally assessed coefficients $Q_{B/C} = 5.0 \pm 0.3$ and $Q_{B/C} = 4.8 \pm 0.7$ as produced in Fig. 4 and 5. In order to display a robust neutron rate with reasonable sensitivity in presence of a low-energy photon background, further investigation on the loading of the scintillators has to be carried out, aiming at reducing the discrepancy in the values for the compensation coefficient below and above 200 keV.

## VIII. Conclusion

A new application of background compensation to neutron detection and counting has been introduced over two small-volume same-geometry gadolinium and bismuth loaded plastic scintillators. The simulation-based loading of the sensors as well as the setting of the parameters for a hypothesis test aiming at discriminating the signature of thermal neutron capture in gadolinium from background statistical fluctuations have been described, resulting in a portable and online implementation-compatible system. The overall detection scheme has then been assessed under neutron and photon radiations. The first quantitative outputs show unbiased countings over conventional natural radioactivity and monitored area typical long-lived product fission backgrounds, with thermal neutron sensitivities promisingly comparable to a similar-active volume commercial He-3 detector.

## IX. Future work

In order to increase the registered count rates on the detection and compensation channels, and therefore the

precision associated to them, future works will be turned towards a scale-up over the loaded scintillating samples, with all the known challenges associated to such a process: homogeneity issues with the loading and self-absorption of the scintillator to quote the more obvious of them [33]. The feasibility of such a scale-up up to 100 $cm^3$ volumes has been established in previous publication for bismuth-loaded and gadolinium-loaded plastic scintillators [20]. However, the pseudo-spectroscopic performances of the scintillating samples, which are necessary to implement countings over selective windows, are still to be enhanced. Once the synthesis for such loaded scintillating samples is stabilized, a systematic study of anisotropy biases, which become more significant for high-scale sensors, will be conducted. As far as the robustness versus sensitivity compromise in the compensation scheme is concerned, the main limitation arises from the distance between the values of the photon compensation coefficient below and above 200 keV. Such distortion originates from the significant difference between effective atomic numbers of the sensors. As a consequence, alternative elements to bismuth will be investigated as dopants for the compensation scintillator.

## REFERENCES


[1] "Chemical, biological, radiological or nuclear (CBRN) detection: a technological overview", NATO Parliamentary Assembly, pp. 18-20 (2005).

[2] "Managing critical isotopes, weaknesses in DOE's management of helium-3 delayed the federal response to a critical supply shortage", GAO-11-472, U.S. Government Accountability Office, Washington, D.C. (2011).

[3] Z. W. Bell, G. W. Brown, C. H. Ho, F. V. Sloop, "Organic Scintillators for Neutron Detection", X-ray and Gamma-ray Detectors and Applications IV, *Proc. of SPIE*, 4784, 150 (2002).

[4] D. A. Abdushukurov, *Gadolinium foils as converters of thermal neutrons in detectors of nuclear radiation*, Physics Research and Technology, p. 7 (2010).

[5] D. A. Shea, "The helium-3 shortage: supply, demand and options for Congress", Congressional Research Service (2010).

[6] S. Normand, V. Kondrasovs, G. Corre, J.-M. Bourbotte and A. Ferragut, "MA-NRBC: First successful attempt for neutron gamma discrimination in plastic scintillators", *Proc. of ANIMMA* (2011).

[7] J R. Hansen, P. Reeder, A. Peurrung and D. Stromswold, "Neutron-gamma discrimination in plastic scintillators", *Nuclear Science Symposium, Conference Record. IEEE*, Vol. 2, pp. 1031-1035 (1998).

[8] G. I. Anisimova, L. S. Danelyan, A. F. Zhigach, V. R. Lazarenko, V. N. Siryatskaya, and P. Z. Sorokin, "Boron-loaded plastic scintillators," *Prib. Tekh. Eksp.*, Vol. 1, pp. 49-51 (1969).

[9] R. D. Breukers, C. M. Bartle, A. Edgar, "Transparent lithium loaded plastic scintillators for thermal neutron detection", *Nuclear Instruments and Methods in Physics Research Section A*, Vol. 701, pp 58-61 (2013).

[10] L. Ovechkina, K. Riley, S. Miller, Z. Bell, V. Nagarkar, "Gadolinium loaded plastic scintillators for high efficiency neutron detection", *Physics Procedia 2*, pp. 161-170 (2009).

[11] E. Velmozhnaya, A. Bedrik, P. Zhmurin, V. Titskaya, A. Adadurov, D. Sofronov, "Investigation of the behavior of gadolinium complexes in plastic scintillators", *Functional materials*, **20**, 4 (2013).

[12] N. P. Zaitseva, M. L. Carman, M. A. Faust, A. M. Glenn, H. P. Martinez, I. A. Pawelczak, S. A. Payne, K. E. Lewis, "System and plastic scintillator for discrimination of thermal neutron, fast neutron and gamma radiation" (2013).

[13] J. Bendahan, E. J. Morton, "Composite gamma-neutron detection system", US 8389941 B2 (2010).

[14] G. Daniel, E. Marienbach, J.–L. Szabo, Commissariat à l'Energie Atomique, "Process and apparatus for the simultaneous selective detection of neutrons and X or gamma photons", US 005481114 (1996).

[15] R. Coulon, J. Dumazert, G. Bertrand, M. Hamel, F. Sguerra, Commissariat à l'Energie Atomique et aux Energies Alternatives, "Dispositif de détection de neutrons et dispositif de comptage de neutrons thermiques associé", FR 1460266 (2014).

[16] www-nds.iaea.org.htm

[17] bricc.anu.edu.au/index.php

[18] *MCNPX User Manual*, Los Alamos Tech. rep., LA-CP-11-00438, 2011.

[19] B. L. Rupert, N. J. Cherepy, B. W. Sturm, R. D. Sanner, S. A. Payne, "Bismuth-loaded plastic scintillators for gamma-ray", *Europhysics Letters*, **97**, 2 (2012).

[20] G. H. V. Bertrand, J. Dumazert, F. Sguerra, R. Coulon, G. Corre and M. Hamel, "Understanding behavior of different metals in loaded scintillators: discrepancy between gadolinium and bismuth", *Journal of Materials Chemistry C*, Vol. 3, pp. 6006-6011 (2015).

[21] G. Knoll, *Radiation Detection and Measurement*, Fourth Edition, John Wiley & Sons, Inc., pp.47-49 (1999).

[22] J. F. Williamson, J. F. Dempsey, A. S. Kirov, J. I. Monroe, W. R. Binns and H. Hedtjärn, "Plastic scintillator response to low-energy photons", *Phys. Med. Biol.*, **44**, 857-871 (1999).

[23] S. A. Pozzi, J. A. Mullens and J. T. Mihalczo, "Analysis of neutron and photon detection position for the calibration of plastic (BC-420) and liquid (BC-501) scintillators", *Nuclear Instruments and Methods in Physics Research Section A*, Vol. 524, pp 92-101 (2004).

[24] R. Coulon, J. Dumazert, V. Kondrasovs, S. Normand, "Nonlinear filter implementing a hypothesis test for online nuclear counting measurements", *Radiation Measurements*, submitted (2015).

[25] R. Coulon, V. Kondrasovs, J. Dumazert, E. Rohée and S. Normand, "Nuclear counting filter based on a Centered Skellam Test and a double exponential smoothing", *Proc. of ANIMMA*, accepted (2015).

[26] $^{252}_{98}$Cf, *Table de radionucléides*, M.-M. Bé, V. Chisté, LNE-LNHB/CEA, 2007.

[27] R. B. Hayes, "Preliminary Benchmarking Efforts and MCNP Simulation Results for Homeland Security", DOE/NV/25946-431, Remote Sensing Laboratory, Las Vegas, NV 89193.

[28] B. Shleien, L. A. Slaback, B. K. Birky, *Handbook of Health Physics and Radiological Health*, 3rd Edition. Lippincott Williams and Wilkins, New York (1998).

[29] Valentine T. E., "Evaluation of Prompt Gamma Rays for Use in Simulating Nuclear Safeguard Measurements", ORNL/TM/-1999/300, Oak Ridge National Laboratory, Oak Ridge, TN (1999).

[30] www.vacutec-gmbh.de/fileadmin/user/Prospekt_He-3_Neutron_Detectors.pdf

[31] M. E. Medhat, Y. Wang, "Estimation of background spectrum in a shielded HPGe detector using Monte Carlo simulations", *Applied Radiation and Isotopes*, **84**, 13-18 (2014).

[32] Légifrance, Arrêté du 15 mai 2006 relatif aux conditions de délimitation et de signalisation des zones surveillées et contrôlées et des zones spécialement réglementées ou interdites compte tenu de l'exposition aux rayonnements ionisants, ainsi qu'aux règles d'hygiène, de sécurité et d'entretien qui y sont imposées (2006), derived from : The 2007 Recommendations of the International Commission on Radiological Protection, ICRP Publication 103, *Ann. ICRP* **37** 2-4 (2007).

[33] J. B. Birks, *The Theory and Practice of Scintillation Counting*, Pergamon Press, pp. 97-98, pp. 185-188 (1964).